ACS APPLIED MATERIALS & INTERFACES

Research Article

www.acsami.org

Nanoscale Heterostructures Based on Fe_2O_3@WO_{3-x} Nanoneedles and Their Direct Integration into Flexible Transducing Platforms for Toluene Sensing

Stella Vallejos,*[,†] Isabel Gràcia,[‡] Eduardo Figueras,[‡] and Carles Cané[‡]

[†]SIX Research Centre, Brno University of Technology, 601 90 Brno, Czech Republic

[‡]Instituto de Microelectrónica de Barcelona (IMB-CNM, CSIC), 08193 Cerdanyola, Barcelona, Spain

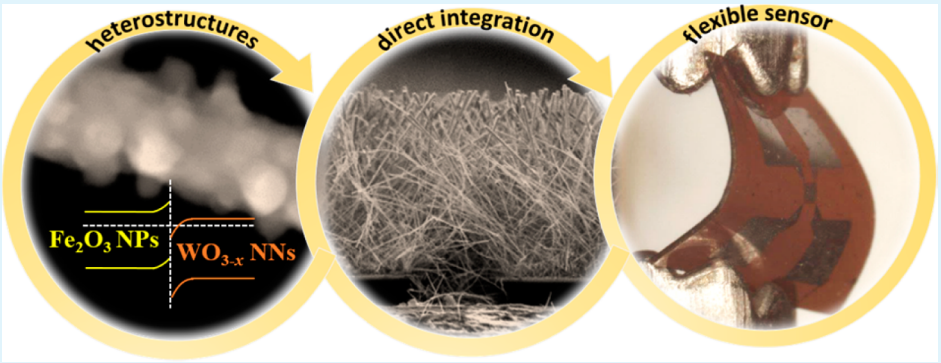

ABSTRACT: Nanoscale heterostructures based on WO_{3-x} nanoneedles functionalized with Fe_2O_3 nanoparticles are integrated directly into flexible polymer-based transducing platforms via aerosol-assisted chemical vapor deposition. Results demonstrate that the incorporation of Fe_2O_3 nanoparticles at the surface of WO_{3-x} nanoneedles enhances the electronic and sensing properties of WO_{3-x}, providing a 6-fold increase in sensitivity to toluene and low cross-sensitivity to hydrogen and ethanol. These enhanced-sensing properties are comparable to those obtained via functionalization with precious metal (Pt) nanoparticles, which are commonly used to enhance sensor performance.

KEYWORDS: *ferric oxide, tungsten oxide, AACVD, flexible gas sensors, toluene*

INTRODUCTION

Metal oxides (MOXs) have broad applications as their properties cover the entire range from metals to semiconductors and insulators. In particular, nanostructured semiconducting MOXs have demonstrated exceptional chemical and physical properties, due to their large number of surface sites, which facilitate surface reactions and electron/phonon confinement. These characteristics have favored the use of these materials in different solid-state devices, including gas sensors.[1]

The optimization of MOXs for gas sensing has been largely studied, particularly with the aim of improving the functionality (i.e., sensitivity, selectivity, stability, and reproducibility) of these materials to eliminate false positives and interfering responses. Consequently, several studies have demonstrated that MOXs (typically n-type such as SnO_2, WO_3, and ZnO) functionalized with second-phase constituents, either nanosized noble metals (e.g., Au, Pt, and Pd) or other n- (e.g., ZnO, SnO_2, and TiO_2) or p-type (e.g., CuO, PdO, and Co_3O_4) MOXs, have a drastic effect on sensing performance, often improving the sensing properties of both the host MOX and the second-phase constituent when the size of these materials is within the Debye length (L_D) of the surface (typically on the order of 2−100 nm) and the second-phase constituents are introduced in small, discrete amounts.[2] Hence, various functionalized MOXs structures (e.g., nanowires (NWs) with second-phase nanoparticles (NPs) at their surface) have being investigated with much interest for gas sensing.

The mechanisms leading to the enhanced performance of these functionalized materials have been attributed to surface- (chemical sensitization) and/or interface- (electronic sensitization) dependent effects.[2−4] To date, there is no clear evidence of which of these mechanisms is more useful for gas sensing, although the literature points to the need to combine both mechanisms to induce an overall better functionality of MOXs.[2] Generally a MOX functionalized with another MOX (i.e., a heterostructure) is more likely to experience surface- and interface-dependent mechanisms during gas detection, while a MOX functionalized with a noble metal is more likely to be dominated by a surface-dependent mechanism.[2,4] The possibility of tuning the sensor performance via these mechanisms will depend strongly on the characteristics of the materials (size, shape, distribution, composition, oxidation

Received: June 9, 2015
Accepted: August 7, 2015
Published: August 7, 2015

DOI: 10.1021/acsami.5b05081
ACS Appl. Mater. Interfaces 2015, 7, 18638−18649

Table 1. Summary of the Synthesis Methods and Utilization of Iron Modified Tungsten Oxide[a]

material	morphology and modification	synthesis method	features, nm	properties	ref
Fe:WO_3	TF [D]	VPS	10−15 [Ø]300 [THK]	Gas sensing (CO)	28
Fe:WO_3	TF [D]	VPS	12 [Ø]100−500 [THK]	Gas sensing (H_2, NH_3, NO_2, N_2O)	29
Fe_2O_3@WO_3	NPs@NPts [F]	WCS	--	Gas sensing (H_2S)	30
Fe_2O_3−WO_3	CBs [M]	WCS	--	Photocatalytic	31
Fe_2O_3−WO_3	TF [M]	WCS	--	Photocatalytic	32
Fe_2O_3−WO_3	TF [M]	VPS	--	Photoelectrochemical	33
Fe_2O_3−WO_3	NPls [M]	VPS	100−200 [Ø]400−500 [LG]	Photoelectrochemical	34
Fe:WO_3	NFks [D]	WCS	--	Photoelectrochemical	35
$(WO_3)_{1-x}$−$(Fe_2O_3)_x$	TF [M]	VPS	32−34 [Ø]200 [THK]	Electrochromical	36
$(WO_3)_{1-x}$−$(Fe_2O_3)_x$	TF [M]	VPS	--	Optical	37
Fe_2O_3−WO_3	NPs [M]	WCS	10−15 [Ø]	Magnetic (after reducing to Fe−W alloy)	38

[a]D: Fe doped film, F: Functionalized (decorated) structures, M: mixture of the two constituents, CBs: cubes, NPls: nanopillars, NPts: nanoplates, NFks: nanoflakes, TF: thin films, Ø: diameter of the grain (particles) or the structure (pillars, plates), LG: length, THK: film thickness.

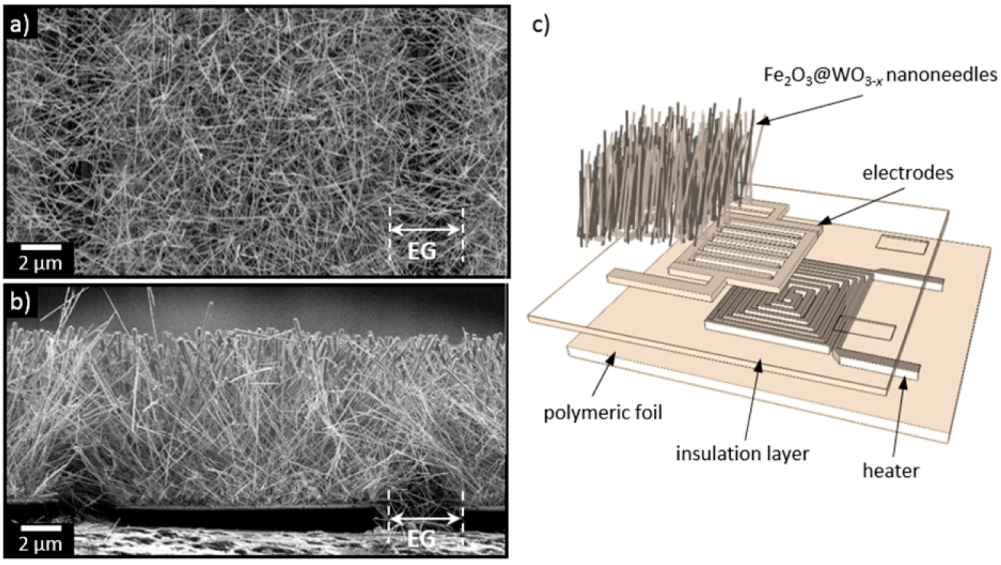

Figure 1. SEM imaging showing the top (a) and section (b) of the microsensor, and schematic view of the layers comprising the flexible gas microsensors (c). EG represents the electrode gap.

states) forming the composite and the creation of an intimate electric contact at the interface of these materials.[2,5,6]

Various conceptual routes to functionalize MOXs with second-phase NPs, based on either liquid-phase or vapor-phase synthesis, are available in the literature. These routes are normally implemented for the fabrication of microdevices via the use of post-transfer (indirect) or direct methods.[7] Synthesizing nanostructured materials in the vapor phase has potential advantages, including the growth of materials with greater purity, higher throughput, and the possibility of integrating materials directly into devices.[8] However, its use for synthesis of nanostructures (e.g., NWs) often requires catalysts (e.g., vapor−liquid−solid approach) and/or relatively high temperatures (~1000 °C), introducing extra fabrication steps and limiting its applicability for their integration with advanced microdevices based either on silicon or on non-conventional substrates (e.g., flexible materials as polymers, textiles, or paper).[9] Against a host of competing enabling technologies for gas sensing with MOX, resistive-based gas sensors attract much interest due to their relative simple architecture, low production cost, and potential to be miniaturized and integrated in personal portable devices for real time analysis. Hence, the significance of this technology for different areas (e.g., indoor quality control[10] or early disease detection[11]), in which portable and real time devices for monitoring gaseous analytes, such as toluene, has gained importance.

Traditionally, the sensitivity of MOXs toward aromatic hydrocarbons in general, and toluene in particular, was reported to be limited. However, with the development of a new generation of nanostructured and functionalized MOXs and the facility of modifying properties such as the concentration of adsorption sites and the energy levels within the material, various nonfunctionalized (e.g., WO_3,[12−15] Fe_2O_3,[16−18] SnO_2,[19,20] ZnO,[21] Co_3O_4[22−24]) and functionalized MOXs nanostructures with metal NPs (e.g., Pt,[14,20] Au,[21] and Pd[15,25]) have shown enhanced sensing performance to aromatic hydrocarbon molecules. From these materials, tungsten oxide has been largely employed for sensing applications and, similarly to SnO_2, it is already used in commercial resistive gas sensors in the form of thin or thick film.[26] Ferric oxide, in contrast, has been generally used for its magnetic properties, although it has also been demonstrated to possess interesting catalytic properties.[27] Particularly, the functionalization of tungsten oxide with iron or iron oxides has shown potential

DOI: 10.1021/acsami.5b05081
ACS Appl. Mater. Interfaces 2015, 7, 18638−18649

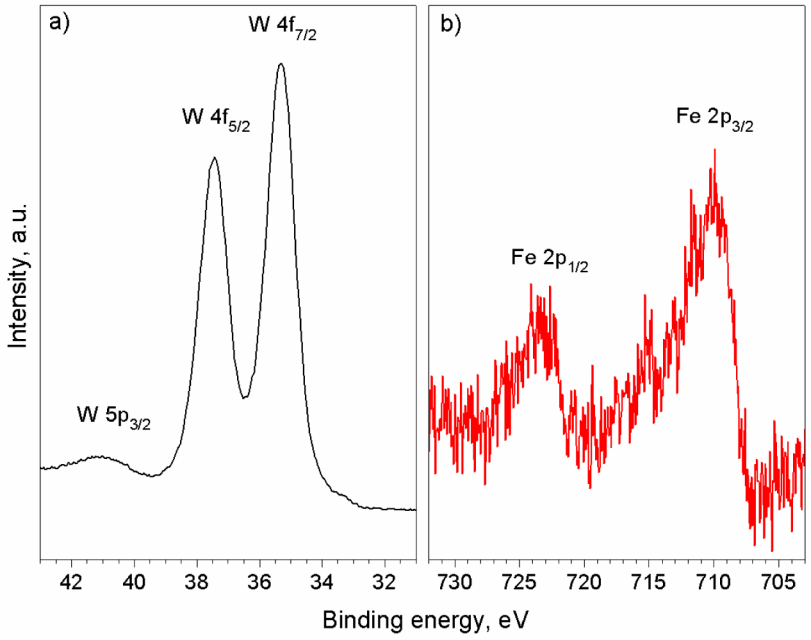

Figure 2. W 4f (a) and Fe 2p (b) XPS core level spectrum recorded on the Fe_2O_3@WO_{3-x} films grown on the polymeric foil.

enhanced gas sensing,[28−30] photocatalytic,[31−35] electrochromical,[36] optical,[37] and magnetic[38] properties (Table 1).

Recently, we have developed a methodology for fabricating flexible functional resistive-based gas microsensors, by combining polymeric-transducing platforms and tungsten oxide nanoneedles (NNs) functionalized with gold or platinum NPs.[39] This methodology consists of the formation of functionalized nanostructures at temperatures compatible with the flexible device using a direct integration approach via a vapor-phase synthesis technique based on aerosol assisted chemical vapor deposition (AACVD).[40,41] Here, we extend this methodology and tune the synthesis of tungsten oxide NNs functionalized with ferric oxide NPs (Fe_2O_3@WO_{3-x}) and their direct integration into polymeric platforms, by achieving the AACVD of Fe_2O_3 from $FeCl_3{\cdot}6H_2O$ at 390 °C. In addition, we compare the functionality of this (Fe_2O_3@WO_{3-x}) system based on n-n nanojunctions with a similar (Pt@WO_{3-x}) system based on n-metal nanojunctions to evaluate the impact produced on the sensing properties of tungsten oxide, when it is functionalized with second-phase NPs of a MOX, instead of a noble metal.

RESULTS

Characterization of the Heterostructures. SEM imaging of the device based on nonfunctionalized (WO_{3-x}) or functionalized (Fe_2O_3@WO_{3-x} and Pt@WO_{3-x}) films showed the films were deposited uniformly on the electrodes forming a mat-like network of nonaligned NNs, interconnected across the electrode gap (EG), with uniform diameters ranging between 50 and 100 nm and lengths of ∼10 μm, i.e., aspect ratios of ∼100 to 200 (Figure 1a,b). A schematic view of the layers comprising the flexible gas microsensor is shown in Figure 1c.

XPS of the films exhibited typical W 4f core level peaks at 35.4 and 37.4 eV (Figure 2a), indicating O/W ratios of 2.8 for the WO_{3-x} films, and 2.7 and 2.6 for the Fe_2O_3@WO_{3-x} and Pt@WO_{3-x} films, respectively (functionalized films showed no contents of chlorine at the surface). The spectra, corresponding to the Pt@WO_{3-x} films, displayed Pt 4f core-level peaks at 74.7 and 71.3 eV with similar characteristics to those observed earlier in similar Pt-functionalized WO_{3-x} NNs synthesized via AACVD,[39,41] whereas the spectra recorded on the films functionalized with Fe_2O_3 displayed Fe 2p core-level peaks at 711.2 and 724.5 eV (Figure 2b), demonstrating the incorporation of iron.[37,42−44] The atomic percentage of iron and platinum found in the Fe_2O_3@WO_{3-x} and Pt@WO_{3-x} films was 3.9 at. % (3.6 wt %) and 3.7 at. % (10.7 wt %), respectively (see Experimental section for details on the adjustment of Fe and Pt content). A comparison of the metal:tungsten ratio present in the initial precursor solution (anal. calcd. for Fe:W 9.8%, Pt:W 18.2%) and the that determined by XPS in the films (found for Fe:W 4.6%, Pt:W 15%) show the incorporation efficiency for iron was 47% and for platinum 79%. This value is much higher compared to the efficiency (10%) obtained previously via wavelength dispersive X-ray (WDX) for the codeposition of Pt@WO_{3-x},[41] likely due to in XPS (a surface analysis technique) the content of platinum appears to be greater than in WDX (a bulk analysis technique).

The presence of satellite peaks for Fe $2p_{1/2}$ and Fe $2p_{3/2}$ that indicate the ionic states of iron are not obvious in the spectrum; however, the binding energies of the Fe 2p peaks and the shape of the $2p_{3/2}$ peak, with apparently no shoulder at lower binding energies (<710 eV), suggest the absence of Fe^{2+}.[37,44] Further analysis of nonfunctionalized films grown via AACVD with only $FeCl_3{\cdot}6H_2O$ dissolved in methanol at 390 °C, support this conclusion, as the Fe 2p core-level peaks of these films (Figure 3a) show a satellite peak at ∼719.4 eV corresponding to Fe^{3+} species,[37,42−44] and the XRD patterns (Figure 3b) indicate diffractions associated with Fe_2O_3 cubic phase (a = 8.351 Å; ICCD card no. 39−1346). These results demonstrate that the AACVD of $FeCl_3{\cdot}6H_2O$ at 390 °C yields ferric oxide films (Figure 3c).

XRD analysis (Figure 4) of the nonfunctionalized and functionalized films suggested the presence of monoclinic phase WO_3 ($P21/n$ space group, a = 7.306 Å, b = 7.540 Å, c = 7.692 Å, and β = 90.88°; ICCD card no. 72−0677), consistent with

DOI: 10.1021/acsami.5b05081
ACS Appl. Mater. Interfaces 2015, 7, 18638−18649

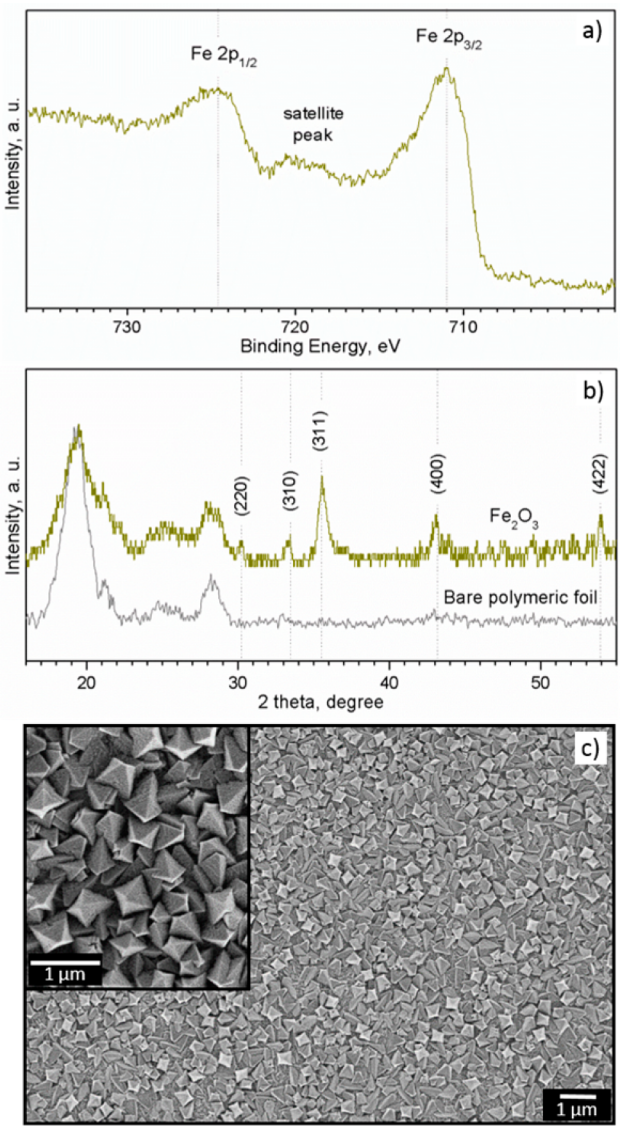

Figure 3. XPS (a), XRD (b), and SEM imaging (c) of the Fe_2O_3 films grown via AACVD on the polymeric foil.

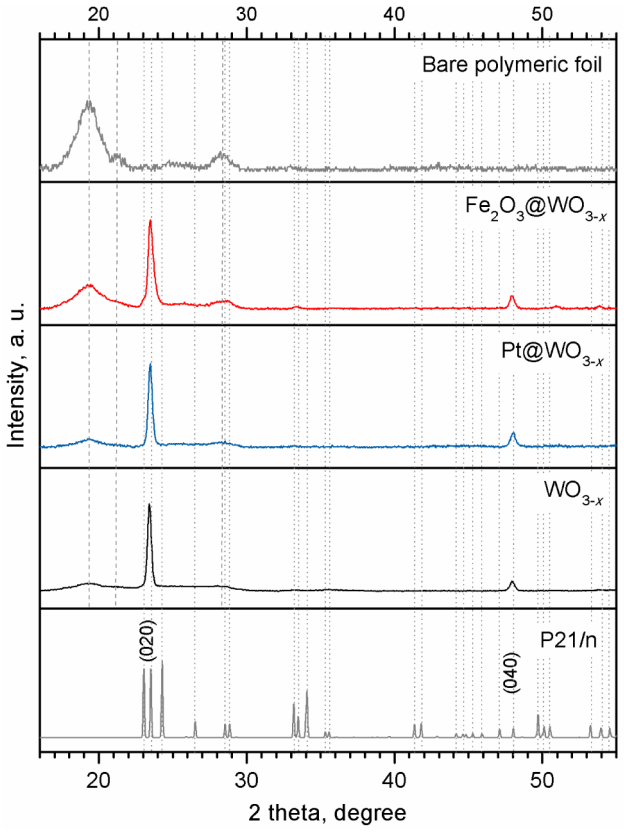

Figure 4. XRD patterns of nonfunctionalized and functionalized tungsten oxide NNs deposited on polymeric foil. Diffraction peaks at 23.57° and 48.23° 2θ in the data are indexed to a monoclinic phase ($P21/n$), ICCD card no. 72−0677.

our previous results for nonfunctionalized or functionalized WO_{3-x} NNs with Au and Pt NPs using either $[W(OPh)_6]$[41] or $W(CO)_6$[39] precursor. Overall, the patterns also exhibit a characteristic background with broad peaks centered at ∼19° 2θ and 28.5° 2θ, coming from the polymeric platform. The intense diffraction peaks at 23.5° 2θ (d = 3.77 Å) and 48.2° 2θ (d = 1.88 Å), corresponding to the (020) and (040) reflections of the monoclinic phase, indicate a strong preferred orientation in the [010] direction. Fe_2O_3 or Pt diffraction peaks were not observed in functionalized films, likely due to the low Fe and Pt contents used for the AACVD.

STEM (Figure 5a and b) and HRTEM (Figure 5c and d) of the NNs functionalized with Fe_2O_3 and Pt showed the presence of dispersed NPs along the surface of the NNs, in contrast to nonfunctionalized NNs, which displayed a bare surface without NPs. EDX of the single functionalized NNs confirmed the presence of tungsten either with Fe or with Pt. Overall, the NNs (nonfunctionalized and functionalized) showed marked planar spacing of approximately 3.55 ± 0.16 Å, which is in agreement with the monoclinic phase identified by XRD (Figure 4) and our prior works on AACVD of $W(CO)_6$.[39,45]

HRTEM of the particles at the surface of the NNs functionalized with Fe_2O_3 showed approximately spherical morphologies (4−15 nm) with certain tendency to form aggregates (Figure 5a). Higher magnification of these NPs (Figure 5c) revealed planar spacing of 2.81 ± 0.15 Å, which is consistent with the internal lattice spacing of the (311) plane of the cubic Fe_2O_3 (d = 2.953 Å, ICCD card no. 39−1346) identified for the films deposited using only $FeCl_3{\cdot}6H_2O$.

The films functionalized with Pt showed smaller (1−5 nm) and more disseminated particles, also with approximately spherical morphologies (Figure 5b), and planar spacing of 2.21 ± 0.11 Å, which correspond to the internal lattice spacing of the (111) plane of face-centered cubic Pt (d = 2.265 Å, ICCD card no. 04−0802) (Figure 5d), consistent with our previous observations for Pt-functionalized structures.[39,41]

The XPS valence-band (VB) spectra recorded near the Fermi level (E_B = 0) on the nonfunctionalized (either WO_{3-x} or Fe_2O_3) and functionalized (Fe_2O_3@WO_{3-x}) films is shown in Figure 6a. A comparison of the linear extrapolation of the VB leading edge[46] of these spectra indicates the simultaneous presence of both WO_{3-x} and Fe_2O_3 induced VB in the Fe_2O_3@WO_{3-x}, with the VB onset for Fe_2O_3 occurring ∼0.9 eV (ΔE_V) above the VB onset for WO_{3-x}. This suggests, according to the literature energy gaps for Fe_2O_3 (2.1 eV) and WO_{3-x} (2.6 eV),[47] that the position of the conduction band (CB) of Fe_2O_3 could be ∼0.4 eV (ΔE_V) above the CB of WO_{3-x} (Figure 6b), producing a staggered type of heterojunction at the interface of the WO_{3-x} NNs and Fe_2O_3 NPs (Figure 6c). Hence, these results show that the presence of Fe_2O_3 NPs at the surface of

DOI: 10.1021/acsami.5b05081
ACS Appl. Mater. Interfaces 2015, 7, 18638−18649

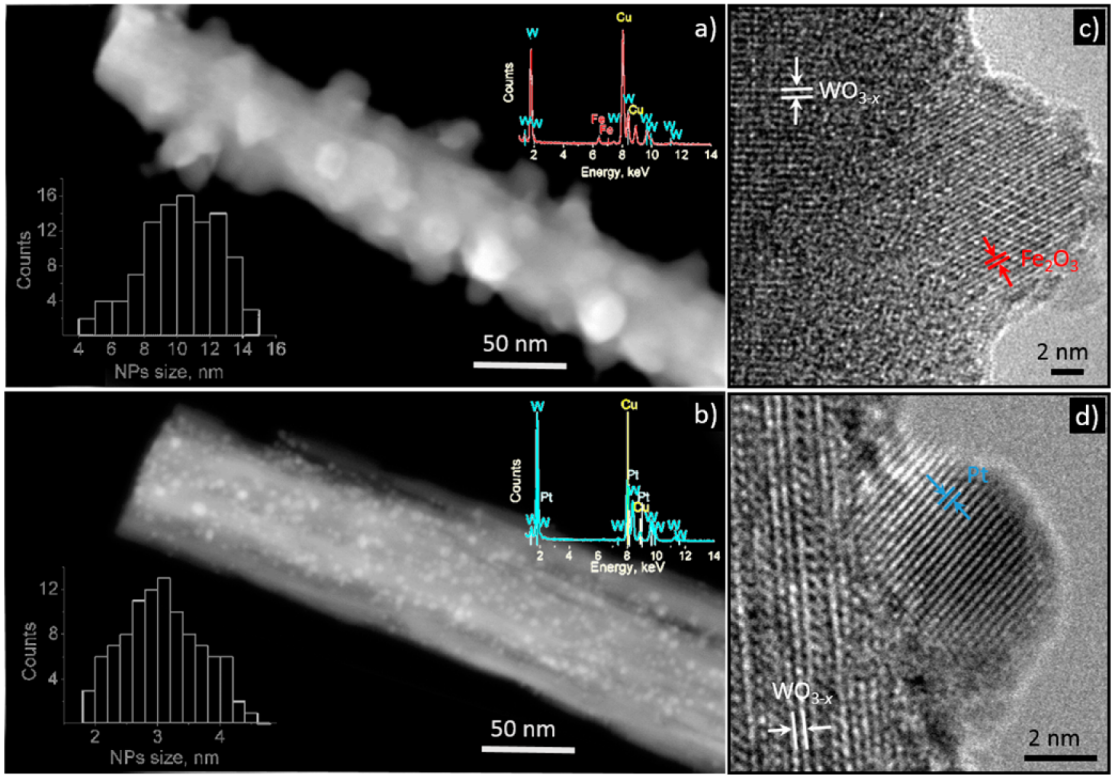

Figure 5. STEM and HRTEM of the WO_{3-x} nanoneedles functionalized with Fe_2O_3 (a, c) and Pt (b, d) NPs. Insets in (a) and (b) display the localized EDX spectra and the dispersion of Fe_2O_3 and Pt NP size.

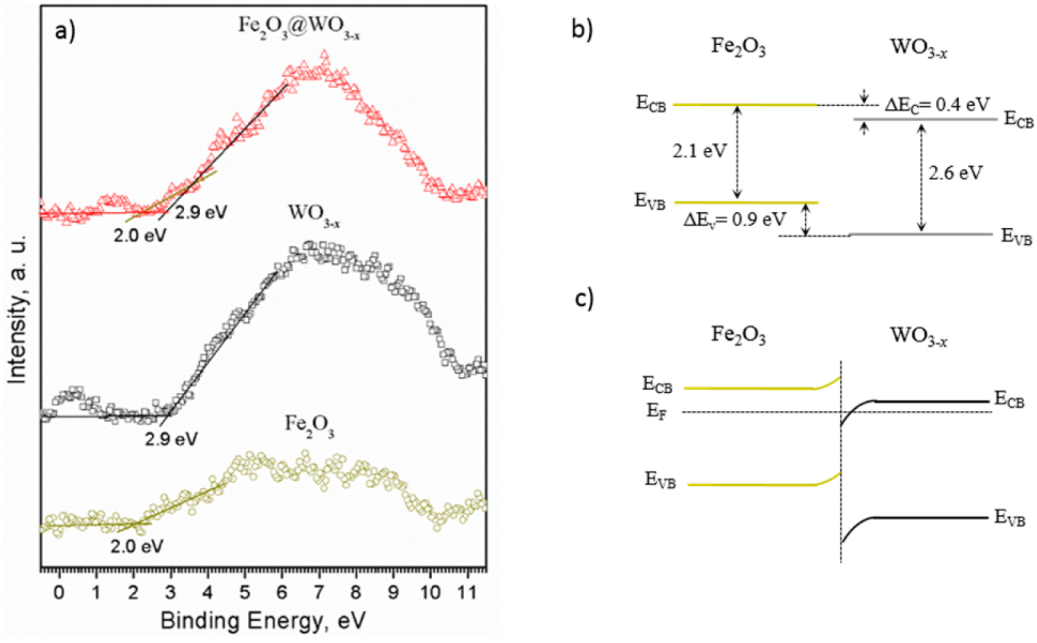

Figure 6. XPS valence band spectra of nonfunctionalized (Fe_2O_3 and WO_{3-x}) and functionalized (Fe_2O_3@WO_{3-x}) films (a), and schematic of the estimated energy level diagram at the interface of Fe_2O_3 NPs and WO_{3-x} NNs (b,c). E_{CB} represents the conduction band minimum, E_F is the Fermi level, and E_{VB} is the valence band maximum (not to scale).

WO_{3-x} NNs leads to new electronic states above the VB maximum of tungsten oxide, increasing the density of electronic states near the Fermi energy level, similarly to that observed previously for Pt@WO_{3-x} films, which also indicated the formation of new electronic states above the VB maximum of the tungsten oxide.[41]

The current (I) − voltage (V) characteristic curves of the films (nonfunctionalized and functionalized), obtained by measuring the electrodes in a continuous flow of nitrogen or dry air at temperatures between 100 and 220 °C, indicated ohmic behavior for each film. As for n-type semiconductors, the electrical resistance of the films showed a direct dependency of the conductivity to the temperature, with the measurements

DOI: 10.1021/acsami.5b05081
ACS Appl. Mater. Interfaces 2015, 7, 18638−18649

under dry air showing larger electrical resistance than those recorded under nitrogen. These resistance changes revealed up to 3-fold increase in nonfunctionalized films and 6-fold increase in films functionalized with Fe_2O_3 or Pt NPs (Figure 7 shows

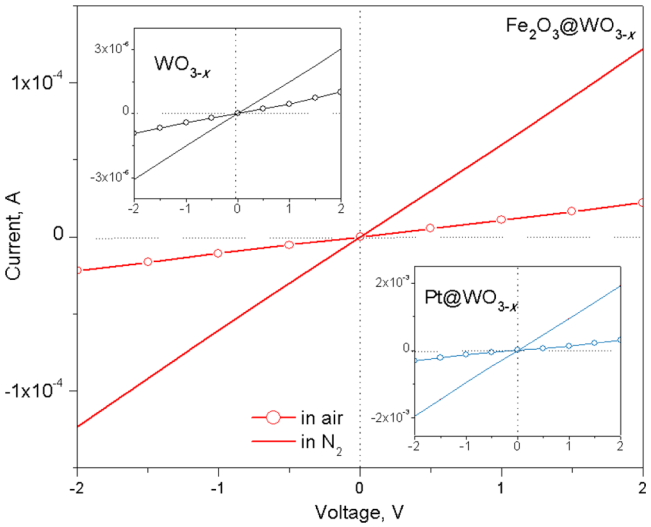

Figure 7. *I*–*V* characteristics in air and N_2 measured via the interdigitated electrodes on the polymeric-transducing platform for the nonfunctionalized and functionalized structures.

an example of the *I*–*V* curves recorded at 220 °C). The activation energy for electrical conduction in air, estimated via the Arrhenius equation, yielded a value of 0.26 eV for nonfunctionalized films, consistent with the apparent energies in air reported for tungsten oxide,[48] whereas the films functionalized with Fe_2O_3 or Pt NPs yielded a value of 0.23 and 0.14 eV, respectively. The energy activation of the films in nitrogen resulted in apparent higher energies, 0.40 eV for nonfunctionalized films, 0.29 eV for Fe_2O_3-functionalized films, and 0.18 eV for Pt-functionalized films.

Sensor Characterization. Gas sensing tests were carried out to toluene, by using dc resistance measurements, at various sensor-operating temperatures from 100 to 250 °C (Figure 8). The sensors displayed an n-type response with decreasing resistance in the presence of toluene and a good reproducibility of the response with little variations of the baseline resistance of the sensors (~1.3%) during the testing period (i.e., 100 h). Figure 9 displays an example of the response replicates

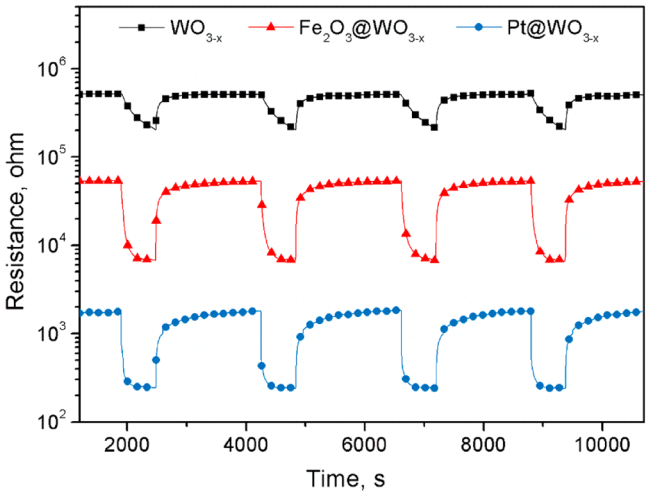

Figure 9. Replicates of the sensor resistance changes toward 100 ppm of toluene at 220 °C.

recorded at 220 °C for toluene. Overall, results indicated better performance for the sensors based on functionalized films as opposed to those based on nonfunctionalized films, with a 2-fold increase in the maximum response recorded (Figure 8a) and faster responses and recovery times (Figure 8b,c). Surprisingly, we found that Fe_2O_3@WO_{3-x} based sensors provided the fastest recovery times.

Further tests of the sensors toward different toluene concentrations showed typical direct dependences of the response to analyte concentration for each material, with closely similar tendencies for sensors based on Fe_2O_3@WO_{3-x} and Pt@WO_{3-x} (Figure 10). Tests to various concentrations (20, 40, 60, 80, 100 ppm) of EtOH and H_2 showed a similar tendency of the response. The sensitivity (defined as the ratio between the change in sensor response for a fixed change in analyte concentration) for each material and analyte is presented in Table 2. These results demonstrate that the functionalization of WO_{3-x} with Fe_2O_3 or Pt NPs improves the sensitivity of WO_{3-x} to toluene and ethanol nearly to the same extent (the sensitivity of the functionalized structures to

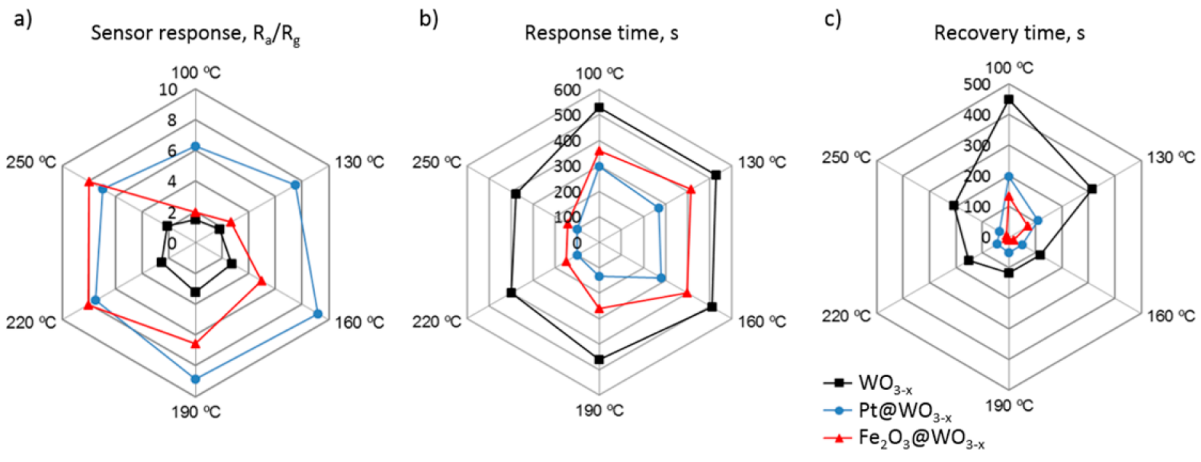

Figure 8. Temperature dependency of the sensor response (a), response time (b), and recovery time (c) for the nonfunctionalized and functionalized sensors.

DOI: 10.1021/acsami.5b05081
ACS Appl. Mater. Interfaces 2015, 7, 18638–18649

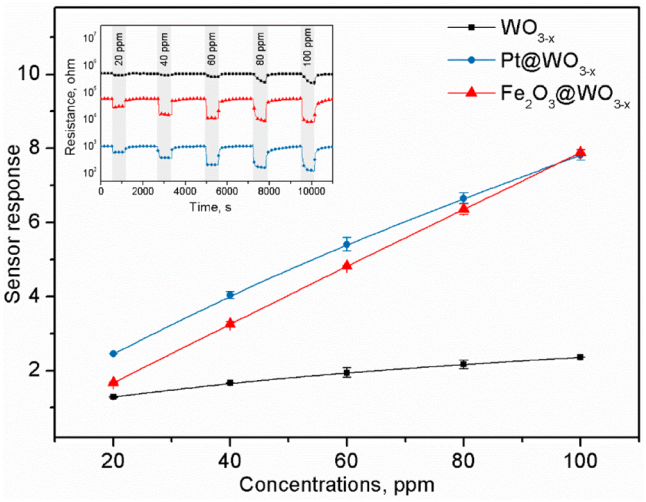

Figure 10. Sensor response in various concentrations of toluene at 220 °C. Inset shows the typical film-resistance changes toward the variation of toluene concentration.

Table 2. Sensitivity of the Nonfunctionalized and Functionalized Structures to Toluene, Ethanol, and Hydrogen at 220 °C

	sensitivity ($\Delta R/\Delta C$)		
	WO_{3-x}	$Pt@WO_{3-x}$	$Fe_2O_3@WO_{3-x}$
Toluene	1.3	6.8	7.6
Ethanol	3.1	4.7	4.2
Hydrogen	4.0	5.6	4.4

toluene and ethanol differs only by 7% and 10%, respectively). In contrast, results for hydrogen suggest that the sensitivity to this analyte increases higher when WO_{3-x} is functionalized with Pt rather than with Fe_2O_3 (the sensitivity of the functionalized structures to hydrogen differs by 22%).

Analysis of variance (ANOVA) of the response for each sensor toward the same concentrations of toluene, ethanol, and hydrogen was performed in order to evaluate the selectivity of the sensors to these analytes (the data set comprise four replicates for each type of sensor and analyte). These results, presented in Figure 11, suggest relatively low cross responses among analytes for each sensor, particularly for the sensors based on $Fe_2O_3@WO_{3-x}$ films, which show a higher difference of the response to toluene in relation to that in ethanol (ΔR = 2.7) or hydrogen (ΔR = 4.2). For comparison, the sensors based on $Pt@WO_{3-x}$ films have a difference of 2.7 or 1.6 in relation to ethanol or hydrogen, respectively, whereas the sensors based on nonfunctionalized WO_{3-x} films have a difference of 1 or 2. These results indicate that $Fe_2O_3@WO_{3-x}$ films have a higher degree of selectivity to toluene in the presence of ethanol and hydrogen.

DISCUSSION

The synthesis of Fe_2O_3 via AACVD has not been investigated extensively in the literature, and the few reports related to the AACVD of this material in its thin film form showed the use of precursors such as $Fe(acac)_3$[49] or $Fe(C_5H_5)_2$[50,51] and iron complexes as $Fe_6(PhCOO)_{10}(acac)_2(O)_2(OH)_{2.3}C_7H_8$.[52] Here we have used a simple iron precursor ($FeCl_3{\cdot}6H_2O$) not reported earlier for AACVD, which has been demonstrated to yield porous Fe_2O_3 films at 390 °C (Figure 3). The formation

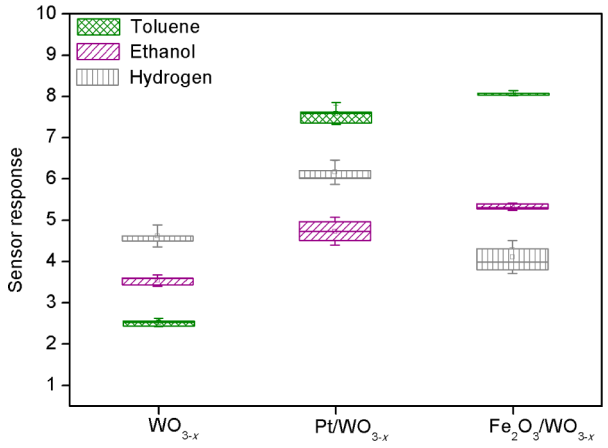

Figure 11. Box plots of the sensor response to 100 ppm of toluene, hydrogen, and ethanol at 220 °C by the nonfunctionalized and functionalized sensors with Fe_2O_3 or Pt NPs. Each box displays the median, mean, and upper and lower quartiles (first and third) of the respective distribution. Box whiskers indicate the standard deviation.

of ferric oxide at this relatively low temperature was appropriate for the codeposition of WO_{3-x} NNs functionalized with Fe_2O_3 NPs (i.e., $Fe_2O_3@WO_{3-x}$) via AACVD and their direct integration with polymeric-transducing platforms (Figure 1). The codeposition of nanostructures with a second-phase constituent via AACVD requires the selection of appropriate conditions (e.g., temperature, precursors, and solvents) so that at the same deposition temperature the first precursor experiences a combination of heterogeneous and homogeneous reactions to encourage the formation of nanostructures, and the second precursor nucleates heterogeneously on the support, or homogeneously in the gas phase with subsequent deposition of NPs on the nanostructure.[40] The present results showed that onset temperature to achieve these conditions when using $W(CO)_6$ and $FeCl_3{\cdot}6H_2O$ as precursors for growing NSs and NPs, respectively, starts at 390 °C (the formation of either tungsten oxide or ferric oxide at this temperature is consistent with the decomposition temperatures of both precursors[53,54]). Based on the morphology of the nonfunctionalized ferric oxide films (Figure 3), it seems that the Fe_2O_3 NPs nucleate heterogeneously on the WO_{3-x} NNs during the codeposition, hence their anchored-like appearance at the NNs and their tendency to form aggregates (Figure 5). The differently sized features of the Fe_2O_3 and Pt NPs at the WO_{3-x} NNs, with bigger particles observed for Fe_2O_3 despite the lower iron precursor concentration used in the initial solution compared to Pt, could be linked in part to the different bulk melting point of these materials (Fe 1811 K; Pt 2042 K).

The electrical characterization (Figure 7) and gas sensing tests (Figures 8 and 9) of the microsensors based on $Fe_2O_3@WO_{3-x}$ NNs indicated an n-type response, consistent with the normal behavior of tungsten oxide and ferric oxide, although transitions from n- to p- type response could also occur for ferric oxide NPs in oxidative environments, as reported previously.[2,55] Due to the differences in the energy bands of WO_{3-x} and Fe_2O_3 (Figure 6), nanoscale heterojunctions emerge at the interface of these materials, inducing electron migration from Fe_2O_3 to WO_{3-x} and the formation of a larger electron density (accumulation layer) in WO_{3-x}, which facilitates additional oxygen adsorption at the functionalized WO_{3-x} NNs surface,[16,23] as supported by the larger resistance changes registered when exposing the $Fe_2O_3@WO_{3-x}$ films to

DOI: 10.1021/acsami.5b05081
ACS Appl. Mater. Interfaces 2015, 7, 18638−18649

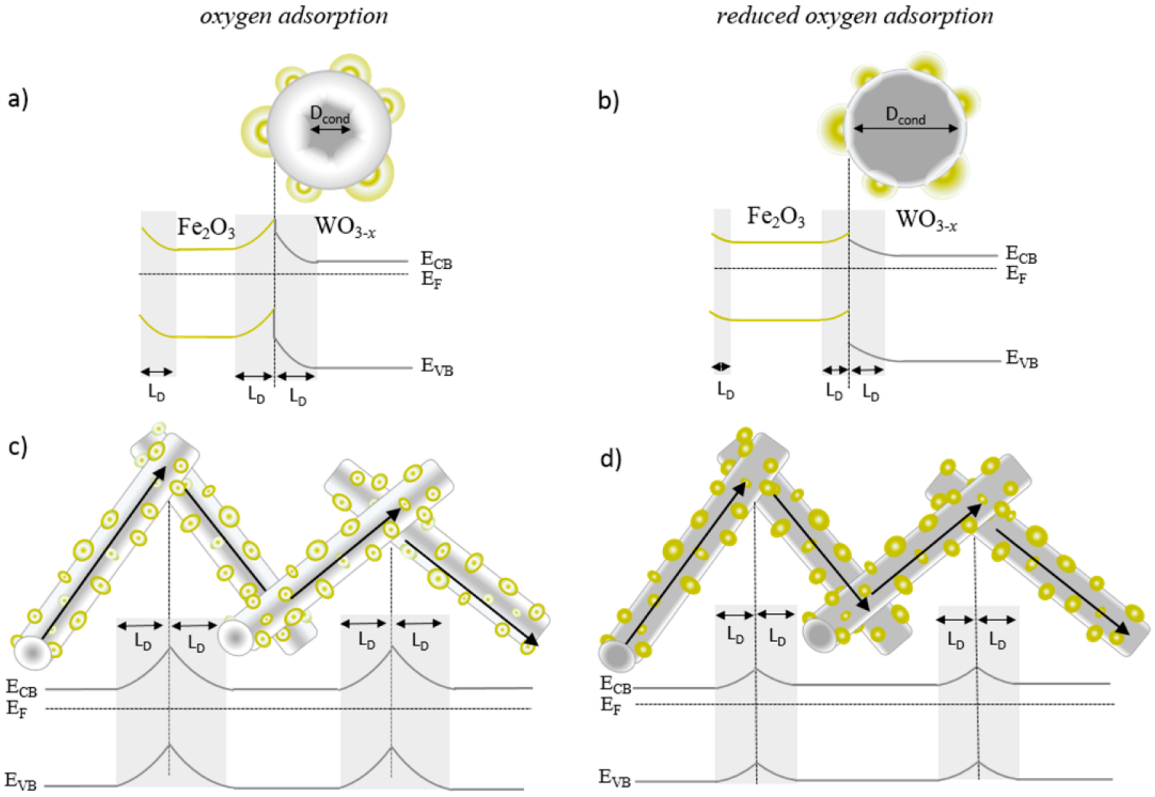

Figure 12. Possible interface-dependent mechanism involved in the gas sensors based on Fe_2O_3@WO_{3-x}. The left side shows the conduction channel mechanism in a NN cross-section (a) and the interfacial mechanism in the film comprising a network of NNs (c) when exposed to air. The right side shows the same mechanisms when the films are exposed to a reducing gas such as toluene, hydrogen, or ethanol (b and d). D_{cond} is the diameter of the nondepleted region available for charge conduction through the core, E_{CB} represents the conduction band minimum, E_F is the Fermi level, E_{VB} is the valence band maximum, and L_D is the Debye length or depth of the depletion region from the surface (not to scale).

N_2 and air (Figure 7). By subsequent oxygen adsorption during exposition of the films to air, the accumulation layer at WO_{3-x} could be depleted, decreasing the conduction channel and as a consequence reducing the conductivity along the NNs. Alternatively, when the functionalized NNs are exposed to reductive analytes, such as toluene, the reductive analyte reacts with the preadsorbed oxygen and releases electrons into the conduction band of the structure, which shrinks the depletion layer, increasing the conduction channel and the conductivity along the NN, as illustrated in Figure 12. Hence, the nanoscale heterojunctions formed at the NNs modulate the conduction channel mechanism of each NN, potentially enhancing the resistance changes during the gas−solid interactions. It is worth noting that in networked NNs films, as those analyzed here, the conductance of the entire film extended across the electrodes of the device depends also on a second interfacial mechanism modulated by the potential barriers originated during oxygen adsorption/desorption at the interface of different NNs (Figure 12c and d). This mechanism is present in nonfunctionalized and functionalized films, although the height of the potential barriers formed at the interface of the NNs is also expected to be influenced by the incorporation of second-phase NPs at the surface of the NNs. The changes in the energy activation of conduction noticed for Fe_2O_3@WO_{3-x} films, in relation to WO_{3-x} films, may be linked to these interface-dependent mechanisms.

The functionalization of the WO_{3-x} with Fe_2O_3 NPs also indicated the presence of a surface-dependent mechanism, which could coexist with the interfacial mechanism enhancing the effects at the heterojunction of these functionalized material. The surface effects on the Fe_2O_3@WO_{3-x} films may include complementary decomposition of the analyte due to the different redox properties of WO_{3-x} and Fe_2O_3,[2] with likely spillover of the gas reaction products, which in the case of toluene involve molecules such as benzaldehyde (C_6H_5CHO) and carbon dioxide (CO_2), among other intermediate products.[16,25,56] The faster response and recovery times (Figure 8b) recorded for functionalized films compared to the nonfunctionalized films give evidence of the presence of surface-dependent mechanisms.

Similar enhancing surface- and interface-dependent mechanisms could also be present in the Pt@WO_{3-x} films, with the interface mechanisms in this system being dominated by a metal/semiconductor junction. However, based on our previous results, which indicated that the Pt NPs introduced via codeposition could contain platinum oxidized states at the Pt/WO_{3-x} junction,[41] the presence of "extra" potential barriers at the interface of these materials is not ruled out.

In general, we noticed that the gas sensing enhancement mechanisms discussed above are apparently not influenced by the size features of the second-phase NPs at the surface, as the functionality of the sensors based on the Fe_2O_3@WO_{3-x} and Pt@WO_{3-x} NNs improves nearly to the same extent, despite the larger size of the Fe_2O_3 NPs relative to Pt NPs.

From the output characteristics of the flexible gas sensing devices based on Fe_2O_3@WO_{3-x} and Pt@WO_{3-x} films, it is concluded that both materials show good performance for toluene, particularly at temperature above 220 °C, in which the sensors showed more stable baseline resistance and faster response and recovery times. Particularly, it is noticed that the

DOI: 10.1021/acsami.5b05081
ACS Appl. Mater. Interfaces 2015, 7, 18638−18649

Table 3. Summary of the Material, Transducing Platforms, and Testing Conditions Reported for Toluene Sensing[a]

material	morphology and modification	method/integration	platform	T_{op} °C	C ppm	R_a/R_g	ref.
WO_3	**NNs**	**VPS/direct**	**Flex^P**	**250**	**100**	**2.2**	**This work**
Pt@WO_3	**NPs@NNs ^{F}**					**7**	
Fe_2O_3@WO_3	**NPs@NNs ^{F}**					**8**	
WO_3	NPs	VPS/direct	Si−μM^P	300	200	3.8	12
WO_3	NNs					6.2	
WO_3	NPs	VPS/direct	Quarz^P	300	10	1.5	13
WO_3	TF	WCS/transfer	Ceramic ^{P}	300	2	1	14
Pt−WO_3	TF ^{M}					1.8	
WO_3	NFs	WCS/transfer	Ceramic^P	350	1	1.2	15
Pd@WO_3	NPs@NFs ^{F}					3.8	
Fe_2O_3	NSs	WCS/transfer	Ceramic^T	440	100	2.3	16
Fe_3O_4−NiO	Coreshell ^{F}	WCS/transfer	Ceramic^T	280	100	13	17
Fe_2O_3@NiO	NRs@NFls ^{F}	WCS/transfer	Ceramic^T	300	100	18.7	18
SnO_2	MC	WCS/transfer	Ceramic^T	280	100	12	19
SnO_2	NFs	WCS/transfer		300	2	1	20
Pt@SnO_2	NPs@NFs ^{F}					1.5	
Pd@SnO_2	NPs@NFls ^{F}	WCS/transfer	Ceramic^T	275	100	17.4	25
SnO2	NFls					1	
Au@ZnO	NPs@NWs ^{F}	WCS/transfer	Ceramic^T	340	100	8.7	21
ZnO	NWs					6.5	
Co_3O_4	NPs	WCS/transfer	Ceramic^T	150	100	12	22
Co_3O_4	NRs	WCS/transfer	Ceramic^T	200	100	25	23
Co_3O_4	NPs					3	

[a]F: Functionalized (decorated) structures, M: mixture of the two constituents, WCS: Wet-chemical synthesis, VPS: Vapor-phase synthesis, NSs: nanoshuttles, NFls: nanoflowers, MC: microcubes, P and T: planar and tube architecture, $R = R_a/R_g$.

recovery times are further improved when functionalizing the WO_{3-x} NNs with Fe_2O_3 NPs, instead of Pt NPs which were also seen to prolong the recovery times in our previous studies.[39] We also notice that the use of Fe_2O_3 NPs, for the functionalization of WO_{3-x} NNs and detection of toluene, could bring potential advantages over the use of Pt NPs due to the lower cross sensitivity to other reductive analytes and the higher temperature dependency of the sensor response, which could favor the use of this material in temperature modulated sensors.[57] Generally, it was noticed that at 250 °C the response of our flexible sensors is higher than those reported in the literature for conventional sensors based on tungsten oxide or ferric oxide systems, and comparable to other sensors based on nonfunctionalized or functionalized MOXs (Table 3), although it is worth mentioning that a comparison of our devices and those in the literature is complex, as the overall performance of the devices is not only linked to the sensing material, but also to other factors including the characteristics of the sensor transducing platform and the test conditions (e.g., operating temperature, flows, and gas concentrations). An interesting point, also noticed in Table 3, is that the most frequent methods used for the fabrication of nanomaterial-based devices typically involve wet-chemical processes assisted by transfer steps to integrate the structures in the device, despite the fact that these multistep processes have demonstrated limited compatibility with architectures desired for multipurpose microelectronic devices. Currently, the need to use scalable and industrially relevant techniques for the integration of highly functional materials and advanced microelectronic devices is one of the less-considered challenges when studying chemically based sensors. This reinforces the added value of this work, which demonstrates the use of a scalable synthesis method that allows the direct integration of functionalized structures into nonconventional microdevices via a single-step process.

In summary, these results demonstrate that the codeposition method developed previously for incorporating metal NPs at the surface of a metal oxide nanostructure[40] can be further extended for the incorporation of second-phase MOX NPs and the formation of nanoscale heterojunctions along a MOX nanostructure. In this work, the incorporation of Fe_2O_3 NPs at the surface of WO_{3-x} NNs has been shown to improve the gas sensor functionality of WO_{3-x} NNs to various reductive gases, particularly to toluene, to nearly the same extent as Pt@WO_{3-x} NNs. The use of Fe_2O_3@WO_{3-x} NNs provides high performance gas sensing devices avoiding expensive and less abundant platinum.

CONCLUSIONS

WO_{3-x} NNs functionalized with Fe_2O_3 NPs were synthetized and integrated directly with flexible transducing platforms using a codeposition method via AACVD at 390 °C. The gas sensing properties of the flexible gas sensors based on Fe_2O_3@WO_{3-x} films demonstrated increased responses to toluene, hydrogen, and ethanol at 220 °C, with up to 6-fold increase in sensitivity to toluene, compared to WO_{3-x} NNs alone, and low cross-response (ΔR) to hydrogen (ΔR = 4.2) and ethanol (ΔR = 2.7). These output characteristics were similar to those recorded for sensors based on Pt@WO_{3-x} NNs, demonstrating that the use of Fe_2O_3 provides almost the same enhancement as the precious metal Pt. The enhanced gas sensing mechanisms of the Fe_2O_3@WO_{3-x} films are linked to surface- and interface-dependent effects, reflected by the changes in both the apparent energy activation of conduction and the sensing response times observed on the Fe_2O_3@WO_{3-x} films, compared to WO_{3-x} alone.

DOI: 10.1021/acsami.5b05081
ACS Appl. Mater. Interfaces 2015, 7, 18638−18649

EXPERIMENTAL SECTION

AACVD of Nanostructures. Briefly, the adjustment of conditions for growing Fe_2O_3@WO_{3-x} or Pt@WO_{3-x} NNs using a codeposition method via AACVD[40] involved a screening of temperatures (325, 350, 375, and 390 °C) finding the onset temperature for the formation of tungsten oxide NNs from 350 °C and the effective incorporation of the second-phase NPs (i.e., Fe_2O_3 or Pt) at 390 °C. In this context, the structures studied in this work were synthetized at 390 °C, and due to the thermal restrictions imposed by the polymeric foils, the AACVD of these precursors at higher temperatures was not investigated. Consequently, the tungsten oxide NNs functionalized with ferric oxide were codeposited via AACVD of a solution containing tungsten hexacarbonyl (20 mg, $W(CO)_6$), Sigma-Aldrich, ≥97%) and ferric chloride hexahydrate (3 mg, $FeCl_3{\cdot}6H_2O$, Sigma-Aldrich, ≥99.6%) dissolved in methanol (5 mL, Sigma-Aldrich, ≥99.9%). As these conditions yielded Fe_2O_3@WO_{3-x} films with iron atomic percentage below 5% (found for Fe 3.9 at.% via XPS), consistent with the low contents recommended to improve the functionality of gas sensing materials,[2,58] for comparison purposes, the AACVD of Pt@WO_{3-x} was adjusted to yield similar platinum atomic percentage (found for Pt 3.7 at.% via XPS), finding the appropriate conditions when using a solution of $W(CO)_6$ (20 mg) and hexachloroplatinic acid hydrate (4 mg, $H_2PtCl_6{\cdot}xH_2O$, Sigma-Aldrich, 99.9%) dissolved in methanol (5 mL). Nonfunctionalized tungsten oxide NNs (WO_{3-x}) or ferric oxide films (Fe_2O_3), in contrast, were deposited from a solution containing only $W(CO)_6$ (20 mg) or $FeCl_3{\cdot}6H_2O$ (80 mg) both dissolved in 5 or 10 mL of methanol, respectively. The aerosol droplets were transported to the heated substrate using a nitrogen gas flow (200 sscm). The time taken to transport the entire volume of solution was typically about 45 min for the 5 mL solution. Plain polymeric foils (Upilex-S, 125 μm, UBE) were used for film analysis, whereas flexible transducing platforms based on the same polymeric foils were used for gas sensor fabrication (see fabrication process in next section). Generally, the AACVD of $W(CO)_6$ or $W(CO)_6$ coreacted with $FeCl_3{\cdot}6H_2O$ or $H_2PtCl_6{\cdot}xH_2O$ resulted in the formation of adherent uniform films with a blue color as-deposited, but after annealing at 390 °C for 1 h with a constant flow of air (50 sscm), nonfunctionalized films became pale blue, whereas functionalized films with Fe_2O_3 and Pt became pale yellow and gray, respectively.

Flexible Transducing Platforms. The flexible polymeric-based transducing platforms were fabricated using commercial high heat resistant polyimide (Upilex-S, 125 μm, UBE). Clean room processes were carried out at the wafer level and consisted of the following main technological steps: patterning of a double loop heater (Ti/Pt, 25 nm/250 nm), deposition and contact opening of an interlevel polymeric layer (U-Varnish, 1 μm, UBE), and patterning of the electrodes (Ti/Pt, 25 nm/250 nm) with a gap of 5 μm. A shadow mask was used during the AACVD process in order to protect the contacts and confine the film deposition to the electrode area (Figure 1a). Bending of the device, before and after AACVD deposition, showed no visible detachment of the electrode or the sensing structures indicating the layers comprising the device had relatively strong adherence to the polymer. More details of the fabrication process and the thermal and bending properties of the flexible platforms were reported earlier.[39,45]

Material Analysis. The morphology of the films was examined using scanning electron microscopy (SEM — Carl Zeiss, Auriga Series, 3 kV), the film structure using X-ray Diffraction (XRD — Bruker, AXS D8 Advance, Cu Kα radiation operated at 40 kV and 40 mA) and the film chemical composition using X-ray photoelectron spectroscopy (XPS — Phoibos 150 analyzer — SPECS GmbH, Berlin, Germany — in ultrahigh vacuum conditions (base pressure 1×10^{-10} mbar) and a monochromatic Kα X-ray source, 1486.74 eV). Scanning transmission electron microscopy (STEM— FEI Tecnai F20, 200 kV) was performed after removing the film from the polymeric platform by sonication.

Gas Sensing Tests. Gas sensors were tested in a continuous flow (50 sccm) test chamber (10 cm^3 volume). The system was provided of three mass flow controllers (Brooks 5850E), and mixtures of pure synthetic air (3X, Praxair) and either calibrated toluene (C_7H_8, Praxair), hydrogen (H_2, Praxair), or ethanol (EtOH, Praxair) in synthetic air were adjusted in order to obtain the desired concentrations, as described previously.[45] The sensors were exposed to the analytes for 10 min and subsequently the chamber was purged with air until initial baseline resistance was recovered. The whole testing period comprised 100 h during which sensors were tested to the analytes at various operating temperatures (100, 130, 160, 190, 220, and 250 °C) performing up to four replicates for each condition (i.e., analyte, operating temperatures, and analyte concentrations). The sensor response (R) was defined as $R = R_a/R_g$, where R_a is the sensor resistance in air at stationary state and R_g represents the sensor resistance after 10 min of analyte exposure. The electrical resistance of the films were measured using a multimeter (Keithley 2700) configured with 20-channel relay multiplexer.

AUTHOR INFORMATION

Corresponding Author

*E-mail: vargas@feec.vutbr.cz. Tel: +420 541 146 153. Fax: +420 541 146 298.

Author Contributions

The manuscript was written through contributions of all authors. All authors have given approval to the final version of the manuscript.

Notes

The authors declare no competing financial interest.

ACKNOWLEDGMENTS

This work has been supported, in part, by the SoMoPro II Programme, cofinanced by the European Union and the South-Moravian Region, via Grant 4SGA8678, and the Spanish Ministry of Science and Innovation via Grant TEC-2013-48147. Part of this research has used the infrastructures of the SIX Research Centre.

REFERENCES

(1) Comini, E.; Baratto, C.; Faglia, G.; Ferroni, M.; Vomiero, A.; Sberveglieri, G. Quasi-One Dimensional Metal Oxide Semiconductors: Preparation, Characterization and Application as Chemical Sensors. *Prog. Mater. Sci.* **2009**, *54*, 1−67.

(2) Miller, D. R.; Akbar, S. A.; Morris, P. A. Nanoscale Metal Oxide-Based Heterojunctions for Gas Sensing: A Review. *Sens. Actuators, B* **2014**, *204*, 250−272.

(3) McAleer, J. F.; Moseley, P. T.; Norris, J. O. W.; Williams, D. E.; Tofield, B. C. Tin Dioxide Gas Sensors. Part 2.-the Role of Surface Additives. *J. Chem. Soc., Faraday Trans. 1* **1988**, *84*, 441−457.

DOI: 10.1021/acsami.5b05081
ACS Appl. Mater. Interfaces 2015, 7, 18638−18649

(4) Yamazoe, N.; Sakai, G.; Shimanoe, K. Oxide Semiconductor Gas Sensors. *Catal. Surv. Asia* **2003**, *7*, 63−75.
(5) Roldan Cuenya, B.; Kolmakov, A. Nanostructures: Sensor and Catalytic Properties. In *Functional Nanostructures: Processing Characterization and Applications*, Seal, S., Ed.; Springer Science + Business media: New York, 2008.
(6) Koziej, D.; Hubner, M.; Barsan, N.; Weimar, U.; Sikora, M.; Grunwaldt, J.-D. Operando X-Ray Absorption Spectroscopy Studies on Pd-SnO_2 Based Sensors. *Phys. Chem. Chem. Phys.* **2009**, *11*, 8620−8625.
(7) Palgrave, R. G.; Parkin, I. P. Aerosol Assisted Chemical Vapor Deposition Using Nanoparticle Precursors: A Route to Nanocomposite Thin Films. *J. Am. Chem. Soc.* **2006**, *128*, 1587−1597.
(8) Girshick, S. Aerosol Processing for Nanomanufacturing. *J. Nanopart. Res.* **2008**, *10*, 935−945.
(9) Comini, E. Integration of Metal Oxide Nanowires in Flexible Gas Sensing Devices. *Sensors* **2013**, *13*, 10659−10673.
(10) Duarte, K.; Justino, C. I. L.; Freitas, A. C.; Duarte, A. C.; Rocha-Santos, T. A. P. Direct-Reading Methods for Analysis of Volatile Organic Compounds and Nanoparticles in Workplace Air. TrAC. *TrAC, Trends Anal. Chem.* **2014**, *53*, 21−32.
(11) Righettoni, M.; Tricoli, A.; Pratsinis, S. E. Si:Wo3 Sensors for Highly Selective Detection of Acetone for Easy Diagnosis of Diabetes by Breath Analysis. *Anal. Chem.* **2010**, *82*, 3581−3587.
(12) Vallejos, S.; Cumeras, R.; Calaza, C.; Sabate, N.; Figueras, E.; Cane, C.; Gracia, I. Localized Heating to Tungsten Oxide Nanostructures Deposition on Gas Microsensor Arrays Via Aerosol Assisted CVD; The 17th International Conference on Solid-State Sensors, Actuators and Microsystems; Barcelona, Spain; June 16−20, 2013; pp 1166−1169.
(13) Chia-Yen, L.; Lung-Ming, F.; Yu-Hou, S.; Joe-Air, J. A Micro Gas Sensor Based on a Wo3 Thin Film for Aromatic Hydrocarbon Detection; Sensing Technology (ICST), 2011 Fifth International Conference; pp 311−314.
(14) Lee, I.; Choi, S.-J.; Park, K.-M.; Lee, S. S.; Choi, S.; Kim, I.-D.; Park, C. O. The Stability, Sensitivity and Response Transients of ZnO, SnO_2 and WO_3 Sensors under Acetone, Toluene and H_2S Environments. *Sens. Actuators, B* **2014**, *197*, 300−307.
(15) Kim, N.-H.; Choi, S.-J.; Yang, D.-J.; Bae, J.; Park, J.; Kim, I. D. Highly Sensitive and Selective Hydrogen Sulfide and Toluene Sensors Using Pd Functionalized WO_3 Nanofibers for Potential Diagnosis of Halitosis and Lung Cancer. *Sens. Actuators, B* **2014**, *193*, 574−581.
(16) Wang, S.; Wang, Y.; Zhang, H.; Gao, X.; Yang, J.; Wang, Y. Fabrication of Porous α-Fe_2O_3 Nanoshuttles and Their Application for Toluene Sensors. *RSC Adv.* **2014**, *4*, 30840−30849.
(17) Qu, F.; Wang, Y.; Liu, J.; Wen, S.; Chen, Y.; Ruan, S. Fe_3O_4−NiO Core−Shell Composites: Hydrothermal Synthesis and Toluene Sensing Properties. *Mater. Lett.* **2014**, *132*, 167−170.
(18) Wang, C.; Cheng, X.; Zhou, X.; Sun, P.; Hu, X.; Shimanoe, K.; Lu, G.; Yamazoe, N. Hierarchical A-Fe_2O_3/NiO Composites with a Hollow Structure for a Gas Sensor. *ACS Appl. Mater. Interfaces* **2014**, *6*, 12031−12037.
(19) Huang, J.; Wang, L.; Gu, C.; Wang, Z.; Sun, Y.; Shim, J.-J. Preparation of Porous SnO_2 Microcubes and Their Enhanced Gas-Sensing Property. *Sens. Actuators, B* **2015**, *207*, 782−790.
(20) Shin, J.; Choi, S.-J.; Lee, I.; Youn, D.-Y.; Park, C. O.; Lee, J.-H.; Tuller, H. L.; Kim, I.-D. Thin-Wall Assembled SnO_2 Fibers Functionalized by Catalytic Pt Nanoparticles and Their Superior Exhaled-Breath-Sensing Properties for the Diagnosis of Diabetes. *Adv. Funct. Mater.* **2013**, *23*, 2357−2367.
(21) Wang, L.; Wang, S.; Xu, M.; Hu, X.; Zhang, H.; Wang, Y.; Huang, W. A Au-Functionalized ZnO Nanowire Gas Sensor for Detection of Benzene and Toluene. *Phys. Chem. Chem. Phys.* **2013**, *15*, 17179−17186.
(22) Zhao, C.; Huang, B.; Zhou, J.; Xie, E. Synthesis of Porous Co_3O_4 Nanonetworks to Detect Toluene at Low Concentration. *Phys. Chem. Chem. Phys.* **2014**, *16*, 19327−19332.
(23) Wang, L.; Deng, J.; Lou, Z.; Zhang, T. Nanoparticles-Assembled Co_3O_4 Nanorods P-Type Nanomaterials: One-Pot Synthesis and Toluene-Sensing Properties. *Sens. Actuators, B* **2014**, *201*, 1−6.
(24) Jeong, H.-M.; Kim, H.-J.; Rai, P.; Yoon, J.-W.; Lee, J.-H. Cr-Doped Co_3O_4 Nanorods as Chemiresistor for Ultraselective Monitoring of Methyl Benzene. *Sens. Actuators, B* **2014**, *201*, 482−489.
(25) Tian, J.; Wang, J.; Hao, Y.; Du, H.; Li, X. Toluene Sensing Properties of Porous Pd-Loaded Flower-Like SnO_2 Microspheres. *Sens. Actuators, B* **2014**, *202*, 795−802.
(26) Fine, G. F.; Cavanagh, L. M.; Afonja, A.; Binions, R. Metal Oxide Semi-Conductor Gas Sensors in Environmental Monitoring. *Sensors* **2010**, *10*, 5469−5502.
(27) Mohapatra, M.; Anand, S. Synthesis and Applications of Nano-Structured Iron Oxides/Hydroxides − a Review Int. *J. Eng. Sci. Technol.* **2011**, *2*, 127−146.
(28) Ahsan, M.; Tesfamichael, T.; Ionescu, M.; Bell, J.; Motta, N. Low Temperature Co Sensitive Nanostructured WO_3 Thin Films Doped with Fe. *Sens. Actuators, B* **2012**, *162*, 14−21.
(29) Tesfamichael, T.; Ponzoni, A.; Ahsan, M.; Faglia, G. Gas Sensing Characteristics of Fe-Doped Tungsten Oxide Thin Films. *Sens. Actuators, B* **2012**, *168*, 345−353.
(30) Yin, L.; Chen, D.; Feng, M.; Ge, L.; Yang, D.; Song, Z.; Fan, B.; Zhang, R.; Shao, G. Hierarchical Fe_2O_3@WO_3 Nanostructures with Ultrahigh Specific Surface Areas: Microwave-Assisted Synthesis and Enhanced H_2S-Sensing Performance. *RSC Adv.* **2015**, *5*, 328−337.
(31) Xu, Z.; Tabata, I.; Hirogaki, K.; Hisada, K.; Wang, T.; Wang, S.; Hori, T. Preparation of Platinum-Loaded Cubic Tungsten Oxide: A Highly Efficient Visible Light-Driven Photocatalyst. *Mater. Lett.* **2011**, *65*, 1252−1256.
(32) Bi, D.; Xu, Y. Synergism between Fe_2O_3 and WO_3 Particles: Photocatalytic Activity Enhancement and Reaction Mechanism. *J. Mol. Catal. A: Chem.* **2013**, *367*, 103−107.
(33) Kollender, J. P.; Mardare, A. I.; Hassel, A. W. Localized Photoelectrochemistry on a Tungsten Oxide−Iron Oxide Thin Film Material Library. *ACS Comb. Sci.* **2013**, *15*, 601−608.
(34) Zhao, P.; Kronawitter, C. X.; Yang, X.; Fu, J.; Koel, B. E. WO_3-Fe_2O_3 Composite Photoelectrodes with Low Onset Potential for Solar Water Oxidation. *Phys. Chem. Chem. Phys.* **2014**, *16*, 1327−1332.
(35) Zhang, T.; Zhu, Z.; Chen, H.; Bai, Y.; Xiao, S.; Zheng, X.; Xue, Q.; Yang, S. Iron-Doping-Enhanced Photoelectrochemical Water Splitting Performance of Nanostructured WO_3: A Combined Experimental and Theoretical Study. *Nanoscale* **2015**, *7*, 2933−2940.
(36) Azimirad, R.; Akhavan, O.; Moshfegh, A. Z. An Investigation on Electrochromic Properties of $(WO_3)_{1-X}$−$(Fe_2O_3)_X$ Thin Films. *Thin Solid Films* **2006**, *515*, 644−647.
(37) Azimirad, R.; Akhavan, O.; Moshfegh, A. Z. The Effect of Heat Treatment on Physical Properties of Nanograined $(WO_3)_{1-X}$−$(Fe_2O_3)_X$ Thin Films. *Vacuum* **2011**, *85*, 810−819.
(38) Pak, J.-J.; Bahgat, M.; Paek, M.-K. Synthesis and Reduction Behavior of Sol-Precipitated Iron Oxide/Tungsten Oxide Nanoparticles. *J. Alloys Compd.* **2009**, *479*, 613−618.
(39) Vallejos, S.; Gràcia, I.; Bravo, J.; Figueras, E.; Hubálek, J.; Cané, C. Detection of Volatile Organic Compounds Using Flexible Gas Sensing Devices Based on Tungsten Oxide Nanostructures Functionalized with Au and Pt Nanoparticles. *Talanta* **2015**, *139*, 27−34.
(40) Vallejos, S.; Stoycheva, T.; Umek, P.; Navio, C.; Snyders, R.; Bittencourt, C.; Llobet, E.; Blackman, C.; Moniz, S.; Correig, X. Au Nanoparticle-Functionalised WO_3 Nanoneedles and Their Application in High Sensitivity Gas Sensor Devices. *Chem. Commun.* **2011**, *47*, 565−567.
(41) Vallejos, S.; Umek, P.; Stoycheva, T.; Annanouch, F.; Llobet, E.; Correig, X.; De Marco, P.; Bittencourt, C.; Blackman, C. Single-Step Deposition of Au- and Pt-Nanoparticle-Functionalized Tungsten Oxide Nanoneedles Synthesized Via Aerosol-Assisted CVD, and Used for Fabrication of Selective Gas Microsensor Arrays. *Adv. Funct. Mater.* **2013**, *23*, 1313−1322.
(42) McIntyre, N. S.; Zetaruk, D. G. X-Ray Photoelectron Spectroscopic Studies of Iron Oxides. *Anal. Chem.* **1977**, *49*, 1521−1529.

DOI: 10.1021/acsami.5b05081
ACS Appl. Mater. Interfaces 2015, 7, 18638−18649

(43) Yamashita, T.; Hayes, P. Analysis of XPS Spectra of Fe^{2+} and Fe^{3+} Ions in Oxide Materials. *Appl. Surf. Sci.* **2008**, *254*, 2441−2449.
(44) O'Byrne, J. P.; Owen, R. E.; Minett, D. R.; Pascu, S. I.; Plucinski, P. K.; Jones, M. D.; Mattia, D. High CO_2 and CO Conversion to Hydrocarbons Using Bridged Fe Nanoparticles on Carbon Nanotubes. *Catal. Sci. Technol.* **2013**, *3*, 1202−1207.
(45) Vallejos, S.; Gràcia, I.; Figueras, E.; Sánchez, J.; Mas, R.; Beldarrain, O.; Cané, C. Microfabrication of Flexible Gas Sensing Devices Based on Nanostructured Semiconducting Metal Oxides. *Sens. Actuators, A* **2014**, *219*, 88−93.
(46) Katnani, A. D.; Margaritondo, G. Microscopic Study of Semiconductor Heterojunctions: Photoemission Measurement of the Valance-Band Discontinuity and of the Potential Barriers. *Phys. Rev. B: Condens. Matter Mater. Phys.* **1983**, *28*, 1944−1956.
(47) Gratzel, M. Photoelectrochemical Cells. *Nature* **2001**, *414*, 338−344.
(48) Ashraf, S.; Blackman, C. S.; Naisbitt, S. C.; Parkin, I. P. The Gas-Sensing Properties of WO_{3-X} Thin Films Deposited Via the Atmospheric Pressure Chemical Vapour Deposition (APCVD) of WCl_6 with Ethanol. *Meas. Sci. Technol.* **2008**, *19*, 1−9.
(49) Tahir, A. A.; Mat-Teridi, M. A.; Wijayantha, K. G. U. Photoelectrochemical Properties of Texture-Controlled Nanostructured α-Fe_2O_3 Thin Films Prepared by AACVD. *Phys. Status Solidi RRL* **2014**, *8*, 976−981.
(50) Pinault, M.; Mayne-L'Hermite, M.; Reynaud, C.; Pichot, V.; Launois, P.; Ballutaud, D. Growth of Multiwalled Carbon Nanotubes During the Initial Stages of Aerosol-Assisted CVD. *Carbon* **2005**, *43*, 2968−2976.
(51) Upul Wijayantha, K. G.; Saremi-Yarahmadi, S.; Peter, L. M. Kinetics of Oxygen Evolution at α-Fe_2O_3 Photoanodes: A Study by Photoelectrochemical Impedance Spectroscopy. *Phys. Chem. Chem. Phys.* **2011**, *13*, 5264−5270.
(52) Tahir, A. A.; Wijayantha, K. G. U.; Saremi-Yarahmadi, S.; Mazhar, M.; McKee, V. Nanostructured α-Fe_2O_3 Thin Films for Photoelectrochemical Hydrogen Generation. *Chem. Mater.* **2009**, *21*, 3763−3772.
(53) Hor, T. S. A.; Chan, H. S. O.; Leong, Y.-P.; Tan, M.-M. X. Thermogravimetric and Quantitative Studies of the Oxidative Decarbonylation of Tungsten Hexacarbonyl. *J. Organomet. Chem.* **1989**, *373*, 221−228.
(54) Louvain, N.; Fakhry, A.; Bonnet, P.; El-Ghozzi, M.; Guerin, K.; Sougrati, M.-T.; Jumas, J.-C.; Willmann, P. One-Shot Versus Stepwise Gas-Solid Synthesis of Iron Trifluoride: Investigation of Pure Molecular F_2 Fluorination of Chloride Precursors. *CrystEngComm* **2013**, *15*, 3664−3671.
(55) Dinesh, K. A.; Shiv, K. G. *Science and Technology of Chemoresistor Gas Sensors*; Nova Science Publisher, Inc.: New York, 2007.
(56) Schmid, W.; Bârsan, N.; Weimar, U. Sensing of Hydrocarbons with Tin Oxide Sensors: Possible Reaction Path as Revealed by Consumption Measurements. *Sens. Actuators, B* **2003**, *89*, 232−236.
(57) Vergara, A.; Martinelli, E.; Llobet, E.; Di Natale, C. Optimized Feature Extraction for Temperature-Modulated Gas Sensors. *J. Sens.* **2009**, *2009*, 1.
(58) Di Maggio, F.; Ling, M.; Tsang, A.; Covington, J.; Saffell, J.; Blackman, C. Aerosol-Assisted CVD Synthesis, Characterization and Gas Sensing Application of Gold Functionalised Tungsten Oxide J. *J. Sens. Sens. Syst.* **2014**, *3*, 325−330.

DOI: 10.1021/acsami.5b05081
ACS Appl. Mater. Interfaces 2015, 7, 18638−18649